

***Ab initio* study of atomic ordering and spin-glass transition in dilute CuMn alloys**

O. E. Peil

*Condensed Matter Theory Group, Department of Physics and Materials Science,
Uppsala University, SE-75121 Uppsala, Sweden*

A. V. Ruban

*Royal Institute of Technology, Department of Material
Science & Engineering, SE-10044, Stockholm, Sweden*

B. Johansson

*Condensed Matter Theory Group, Department of Physics and Materials Science,
Uppsala University, SE-75121 Uppsala, Sweden and
Royal Institute of Technology, Department of Material
Science & Engineering, SE-10044 Stockholm, Sweden*

Abstract

An archetypical spin-glass metallic alloy, $\text{Cu}_{0.83}\text{Mn}_{0.17}$, is studied by means of an *ab-initio* based approach. First-principles calculations are employed to obtain effective chemical, strain-induced and magnetic exchange interactions, as well as static atomic displacements, and the interactions are subsequently used in thermodynamic simulations. It is shown that the calculated atomic and magnetic short-range order accurately reproduces the results of neutron-scattering experiments. In particular, it is confirmed that the alloy exhibits a tendency toward ordering and the corresponding ordered phase is revealed. The magnetic structure is represented by spin-spiral clusters accompanied by weaker ferromagnetic short-range correlations. The spin-glass transition temperature obtained in Monte Carlo simulations by a finite-size scaling technique, 57 K, is in reasonable agreement with experimental data, 78 K.

I. INTRODUCTION

Spin-glass materials still keep on puzzling researchers with their unusual magnetic properties. Since the beginning of 1970s, when Canella and Mydosh¹ observed a cusp in the temperature dependence of the magnetic susceptibility of a dilute solution of Fe atoms in Au, the theory of spin glasses has become a subject of non-trivial physical and mathematical investigations.² Three years after the initial discovery of the phenomenon, Edwards and Anderson³ attributed the origin of the cusp to the appearance of a spin-glass state, in which the moments of the magnetic atoms are frozen in a disordered, glassy structure. They showed that a substantially simplified model (EA model) could reproduce such a state and the model became a basis for analytical mean-field considerations. However, despite the indisputable success of the mean-field theory to explain many of the spin-glass properties, the connection of the EA model to real experimentally investigated spin-glass materials, such as, for instance, dilute magnetic alloys of Mn and Fe in noble metals (Cu, Ag, and Au), remains in most cases subtle and unclear. A great deal of failure to establish a relation between the mean-field treatment and realistic models can be ascribed to the lack of knowledge of the detailed structure of real materials.

Here, we present a theoretical investigation of the structure and spin-glass behavior of Cu-Mn alloys using a realistic parameter-free model based on first-principles calculations. There is a large amount of experimental information on the structural and spin-glass properties of dilute noble-metal-manganese alloys and specifically in Cu-Mn alloys.^{4,5,6,7,8,9,10,11,12,13,14,15,16,17,18} This especially concerns the atomic and magnetic short-range orders (ASRO and MSRO) in $\text{Cu}_{0.83}\text{Mn}_{0.17}$ alloys which have been intensively investigated by various experimental techniques. In particular, it has been established that the ASRO in $\text{Cu}_{0.83}\text{Mn}_{0.17}$ exhibits maxima at $Q_a = (1, 1/2, 0)$,^{8,9,10,13,19,20} while the MSRO indicates the existence of a strong tendency toward formation of magnetic spin-density wave (SDW) clusters with a wave vector $Q_m = (1, 1/2 \pm \delta, 0)$, where δ is concentration dependent.^{9,11} In addition, static atomic displacements have just recently been investigated by diffuse x-ray scattering in this alloy.²¹ Nevertheless, the detailed atomic and magnetic structures of these alloys at the atomic level are not known. For instance, the experimentally observed ASRO does not allow determining unambiguously the type of atomic ordering. A comprehensive analysis of the most accurate up-to-date experimental data⁸ shows the pres-

ence of elements of several $(1, 1/2, 0)$ -type superstructures: $D1_a$, DO_{22} , and Pt_2Mo , but none of them can be singled out as a candidate for the low-temperature ground-state structure.

Magnetic ordering in these alloys also exhibits quite an unusual behavior. Although the neutron-scattering experiments show strong short-range correlations of the SDW type, no magnetic ordering occurs in the CuMn alloys at low temperatures. Instead, typical traits of a spin glass (SG) are observed: the cusp in the linear susceptibility,²² difference in the zero-field-cooled (ZFC) and field-cooled (FC) magnetizations,²³ frequency dependence of the ac susceptibility,²⁴ etc. All these phenomena are connected to the SG phase transition observed as the divergence of the non-linear susceptibility,²⁵ which is equivalent to the divergence of the SG-susceptibility (see Section VI).²

The mechanism of the onset of the SG behavior in metallic alloys, and in the CuMn alloy in particular, is still unclear. Along with fundamental problems concerning the universality class of a frustrated system with long-range interactions, there is still much to be understood in what concerns the role of magnetic clustering in a SG transition. Indeed, the observation of strong short-range correlations of the SDW type below and above the transition temperature indicates that spin freezing is accompanied by the development of magnetic clusters. There is no doubt that this collective behavior contributes appreciably to the magnetic dynamics near the transition. It is thus necessary to have a clear picture of the magnetic ordering at the atomic scale.

At the same time, comprehensive theoretical investigations, in particular those based on first-principles calculations, of atomic and magnetic orders in Cu-rich Cu-Mn alloys are practically absent. The first *ab initio* calculations of the magnetic exchange interactions in dilute Cu-Mn alloys were performed by Oswald *et al.*²⁶ on the basis of Korringa-Kohn-Rostoker (KKR) impurity Green's function calculations. They showed that the magnetic exchange interactions between Mn atoms in Cu are of the antiferromagnetic type at the first coordination shell, but ferromagnetic at the second and third, explaining thereby the existence of the weak ferromagnetic SRO observed in Cu-Mn alloys.

The type of the magnetic and atomic short range order in Cu-rich Cu-Mn alloys has also been investigated by Ling and co-workers,^{27,28} who calculated the ASRO and paramagnetic susceptibilities in these alloys using a so-called $S^{(2)}$ -formalism with cavity corrections within density functional theory KKR-coherent potential approximation (DFT KKR-CPA).²⁹ However, such a mean-field consideration could not provide information about the

detailed atomic and magnetic structures at the atomic level. Besides, their calculations for the $\text{Cu}_{85}\text{Mn}_{15}$ alloy could reproduce neither splitting of the $(1, \frac{1}{2}, 0)$ magnetic peak nor the ordering tendency for the ASRO, for which they found the phase-separation (or clustering) behavior in direct contradiction to the experimental data.

In this work, we investigate atomic and magnetic orderings in the $\text{Cu}_{0.83}\text{Mn}_{0.17}$ alloy on the basis of corresponding Monte Carlo thermodynamics simulations, with chemical and magnetic interactions being deduced from first-principles calculations. The outline of the paper is as follows: Basic models, methods, and approximations, along with the description of our approach, are presented in Section II. The calculated chemical and strain-induced interactions are analyzed in Section III. In Section IV, the results for the ASRO obtained from Monte Carlo simulations are compared to those provided by experiments. Cooling down below the ordering temperature in the Monte Carlo simulations also allows us to reveal the underlying ordered phase of a dilute CuMn alloy. Monte Carlo magnetic simulations described in Section V provide us with a detailed picture of the magnetic correlations in the system. A more thorough investigation of the SG behavior is presented in Section VI, where we show that the system exhibits a spin-glass transition and examine the critical behavior. We conclude the results in Section VII.

II. METHODOLOGY

Two different types of ordering are of interest in our case: atomic or chemical, describing relative positions of Cu and Mn atoms on the lattice; magnetic, associated with the spin configuration of the Mn atoms. In general, these degrees of freedom can be interconnected in a quite complicated way due to the strong dependence of magnetic interactions on the local chemical environment of magnetic atoms, and owing to the dependence of the chemical interactions on both the local and global magnetic states, as it is the case in, e.g., FeCr alloys.³⁰ However, such an interconnection is relatively weak in Cu-rich Cu-Mn alloys. Besides, the magnetic and atomic ordering effects are well separated in temperature.

At high temperatures relevant for the atomic local ordering, where atomic diffusion is still possible (above 400-500 K), the alloy is in a paramagnetic state with randomly distributed directions of local magnetic moments on Mn atoms. The thermally induced magnetic excitations connected with the fluctuation of the direction of spin magnetic moments on Mn

atoms are several orders of magnitude faster than the atom-vacancy interchange jumps occurring during equilibration of the alloy. It is therefore possible to average out the magnetic degrees of freedom and obtain effective interatomic interactions to describe the alloy thermodynamics at temperatures substantially higher than the spin-freezing temperature. On the other hand, at low temperatures – of the order of 100K and below – where the spin-glass transition is observed, atomic diffusion is practically absent³¹ and magnetic configurations should be determined for the Mn atoms fixed in their positions on the lattice. Two separate problems are thus considered: finding a chemical alloy configuration on the underlying lattice and obtaining the equilibrium ensemble of magnetic configurations for the Mn atoms at a temperature of interest.

A. Atomic configurational Hamiltonian and effective cluster interactions

The chemical, or atomic, configurational Hamiltonian used in the present work is of an Ising type

$$H_{chem} = \frac{1}{2} \sum_{i \neq j} \left(V_{ij}^{(2)} + V_{ij}^{si} \right) \sigma_i \sigma_j + \frac{1}{3} \sum_{i \neq j \neq k} V_{ijk}^{(3)} \sigma_i \sigma_j \sigma_k + \frac{1}{4} \sum_{i \neq j \neq k \neq l} V_{ijkl}^{(4)} \sigma_i \sigma_j \sigma_k \sigma_l, \quad (1)$$

where spin-variables, σ_i , take on values +1 or -1 if a site i is occupied by Mn or Cu atom, respectively. The effective cluster m -site interactions (ECIs), $V_{ij\dots k}^{(m)}$, and the pair strain-induced (SI) interactions, V_{ij}^{si} , are obtained from *ab initio* calculations as described below.

The ECI have been calculated by the screened generalized perturbation method (SGPM) (Ref. 32) on the basis of self-consistent electronic structure calculations of random Cu-Mn alloys by the exact muffin-tin orbital (EMTO) method³³ within the coherent-potential approximation (CPA).³⁴ Since the magnetic structure stabilizes at high temperature in a paramagnetic state, we have used a disordered local-moment (DLM) (Ref. 35) magnetic configuration for Mn atoms, treating the Cu-Mn alloy as a three-component system, Cu-Mn[↑]-Mn[↓], where Mn^{↑,↓} represent spin-up and spin-down alloy components, respectively, with the same number of Mn[↑] and Mn[↓] atoms distributed randomly relative to each other.

The ECIs of a binary alloy are then determined as the corresponding averages of the ECI of the initial three-component alloy (see, for instance, Ref. 32). The intersite screening constants for the screened Coulomb interactions contributing to the pair interactions^{36,37} have been determined by 864-atom supercell calculations of a random Cu_{0.83}Mn_{0.17} alloy in

the ferromagnetic state using the locally self-consistent Green's function (LSGF) method,³⁸ assuming that the screening constants do not depend on the magnetic configuration of Mn atoms.

Although the size mismatch of Cu and Mn atoms is rather moderate (the atomic volume difference of pure γ -Mn in the paramagnetic state and Cu is less than 10%³⁹), and local lattice relaxations should consequently be relatively small and give little contribution to alloy energies, they should be included whenever a quantitative analysis is performed, especially in case of relatively small chemical effective interactions. In order to take the local relaxation effects into account, we have calculated the strongest and most important strain-induced interactions at the first three coordination shells in the dilute limit of Mn in Cu using a supercell approach as

$$V_{ij}^{\text{si}} = E_{ij,\text{rel}}^{(2)} - E_{ij,\text{unrel}}^{(2)} - 2(E_{\text{rel}}^{(1)} - E_{\text{unrel}}^{(1)}), \quad (2)$$

where $E^{(1)}$ and $E_{ij}^{(2)}$ are the total energies of supercells with a single Mn impurity and with a corresponding pair of Mn impurities in pure Cu. Indices "rel" and "unrel" designate energies for the relaxed and unrelaxed supercells (only atomic positions are allowed to relax, the volume and shape of the supercells are kept fixed).

The total energies have been calculated by the projector augmented wave (PAW) method^{40,41} within the local density approximation (LDA)^{42,43} as it is implemented in the Vienna *ab initio* simulation package (VASP).^{44,45,46} The plane-wave cut-off energy was set to 330 eV. If a structure has been optimized, the internal structural parameters have been relaxed until the Hellman-Feynman forces on each atom are less than 0.001 eV/Å. Two 108-, and 256-atom supercells have been used to check the convergence with respect to the supercell size. The presented results have been obtained for the *room-temperature experimental* lattice spacing of 3.6792 Å,³⁹ unless a different lattice spacing is specified.

B. Magnetic Hamiltonian and exchange interaction parameters

A Heisenberg-type Hamiltonian has been used in magnetic statistical thermodynamics simulations

$$H = - \sum_{ij} J_{ij} c_i c_j \mathbf{e}_i \mathbf{e}_j, \quad (3)$$

where \mathbf{e}_i is a unit vector in the direction of the local magnetic moment at a site i and J_{ij} the magnetic exchange interaction parameters. The occupation numbers, c_i , take on values 1 or 0 if the Mn or Cu atom occupies a site i , respectively, [occupation numbers are related to σ_i in the Hamiltonian (1) as $c_i = (1 - \sigma_i)/2$]. The occupation numbers in the Heisenberg Monte Carlo simulations have been taken for an alloy configuration obtained from an atomic Ising Monte Carlo simulation. The magnetic exchange interaction parameters between Mn atoms in the alloy have been calculated using the magnetic force theorem formalism⁴⁷ implemented within the EMTO method. The validity of the Heisenberg description has been checked by comparing interactions obtained in the DLM, ferromagnetic, and antiferromagnetic states, as well as by comparing the results of the PAW supercell calculations with the EMTO magnetic force theorem results, as described below.

We have also investigated the influence of the local environment effects and ASRO on the magnetic exchange interactions for a $\text{Cu}_{0.75}\text{Mn}_{0.25}$ alloy. Two supercells have been generated: one representing a completely random alloy (the SRO parameters up to the tenth coordination shell are kept close to zero) and another one with the SRO parameters set to equal those obtained from an alloy Monte Carlo simulation for 300K (the SRO parameter at the first coordination shell, $\alpha_1 \approx -0.1$). The electronic structure of both supercells has been calculated by the LSGF method.³⁸ The magnetic exchange interaction parameters in these supercells have been calculated for different pairs of Mn atoms having different numbers of Cu and Mn atoms at the first coordination shell. The relative variation of the nearest-neighbor exchange interaction parameter J_1 has been found to be less than 5% for most of the pairs. The relative difference between the average values of J_1 for different SROs turns out to be even less significant. The exchange interactions at larger coordination shells proved to be almost insensitive to the local environment and SRO effects. We can thus conclude that the fixed values of the exchange interaction parameters, independent of the local chemical environment and global ASRO, can safely be used in magnetic Monte Carlo simulations.

III. EFFECTIVE CLUSTER INTERACTIONS IN $\text{Cu}_{0.83}\text{Mn}_{0.17}$ ALLOY

A. Chemical interactions

The calculated, as described in the previous section, total, chemical and, strain-induced interactions are shown in Fig. 1. The values of the bare (unscreened) chemical interactions at the first two coordination shells are shown to emphasize the importance of screening effects in the system. As one can see, the correct account of the electrostatic contribution leads to the change of the interaction sign at the first coordination shell. An appreciable part of the concentration and lattice-constant (at 17 at % Mn) dependence of the interaction at the first coordination shell (depicted in Figs. 2 and 3) is due to the one-electron energy contribution. The values of the effective cluster interactions up to the 80th coordination shell, which have been considered in the statistical thermodynamic simulations, are listed in Table V.

A relatively large screening contribution to the chemical interaction at the first coordination shell suggests that the value of the interaction is quite sensitive to the screening parameter, which can, in fact, be quite inaccurate due to the use of the atomic sphere approximation even with the multipole moment correction taken into account. The accuracy of the SGPM interaction at the first coordination shell has, therefore, been checked in supercell calculations. This can be easily done in the dilute limit by considering, for instance, a nearest-neighbor pair of Mn atoms in a large sample of Cu. The total interaction energy related to the effective pair interaction in this case is

$$V_{tot}^{Mn-Mn} = \frac{1}{4} (E^{\text{Mn-Mn}} - 2E^{\text{Mn}} + E^{\text{Cu}}), \quad (4)$$

where $E^{\text{Mn-Mn}}$ is the total energy of a supercell with two Mn atoms (in this particular case separated by one coordination shell), E^{Mn} the total energy of the same supercell but containing only a single Mn atom, and E^{Cu} the total energy of pure Cu (normalized on the same supercell). The prefactor 1/4 is due to the definition of the Ising Hamiltonian (1).

In a magnetic system, Eq. (4) leads to two different types of interactions, depending on the relative orientation of the magnetic moments of the Mn atoms: ferromagnetic (FM), $V_{tot}^{\text{Mn}\uparrow-\text{Mn}\uparrow}$, and antiferromagnetic (AFM), $V_{tot}^{\text{Mn}\uparrow-\text{Mn}\downarrow}$. The interactions are calculated from the total energy of the ferromagnetic, $E^{\text{Mn}\uparrow-\text{Mn}\uparrow}$, or antiferromagnetic, $E^{\text{Mn}\uparrow-\text{Mn}\downarrow}$, state, respectively. However, the interaction $V^{(2)-\text{GPM}}$ is calculated in the DLM magnetic state, and in order to compare this interaction with $V_{tot}^{\text{Mn-Mn}}$, proper averaging of the latter over all

possible spin configurations of the pair must be performed. The interaction in the DLM state, relevant to our consideration at temperatures above the spin-glass transition, is therefore given by the following average:^{30,32}

$$V_{\text{tot-DLM}}^{\text{Mn-Mn}} = \frac{1}{2} \left(V_{\text{tot}}^{\text{Mn}\uparrow\text{-Mn}\downarrow} + V_{\text{tot}}^{\text{Mn}\uparrow\text{-Mn}\uparrow} \right). \quad (5)$$

At the same time, the difference of these two interactions is the magnetic exchange interaction parameter of the Heisenberg magnetic Hamiltonian (3) at the corresponding coordination shell

$$J_{ij} = V_{\text{tot}}^{\text{Mn}\uparrow\text{-Mn}\downarrow} - V_{\text{tot}}^{\text{Mn}\uparrow\text{-Mn}\uparrow}, \quad (6)$$

where i and j are the position indices of the Mn atoms in the lattice.

Besides, one should bear in mind that the interaction energy $V_{\text{tot}}^{\text{Mn-Mn}}$ includes all the multi-site contributions present in the system and they should be subtracted before a comparison with the chemical part of the effective pair interaction is carried out

$$V_{\text{sc}}^{(2)} = V_{\text{tot}}^{\text{Mn-Mn}} - \frac{1}{4} \Omega^{\text{multi}}, \quad (7)$$

where Ω^{multi} is the multi-site contribution corresponding to the right-hand side of Eq. (4). It can be obtained using the GPM multi-site interactions, calculated in the dilute limit; the multi-site interactions are usually sufficiently accurately reproduced by the GPM since they do not contain an electrostatic contribution. Although the multi-site interactions are relatively weak (some of the strongest three- and four-site interactions for the $\text{Cu}_{0.83}\text{Mn}_{0.17}$ alloy are listed in Tables VI and VII) they contribute appreciably to Ω^{multi} as one can see in Table I.

TABLE I: Interaction energies for a pair of Mn atoms in the dilute limit obtained from the GPM ($V^{(2)\text{-GPM}}(c_{\text{Mn}} \rightarrow 0)$) and from supercell calculations, $V_{\text{sc}}^{(2)}$. All energies are given in mRy. The parameters $V^{\text{Mn-Mn}}$ are calculated according to Eq. (4); Ω^{multi} is the multi-site contribution.

$V^{(2)\text{-GPM}}$	$V_{\text{sc}}^{(2)}$	$V^{\text{Mn}\uparrow\text{-Mn}\downarrow}$	$V^{\text{Mn}\uparrow\text{-Mn}\uparrow}$	J_1	Ω^{multi}
1.085	1.105	-0.728	3.040	-3.77	0.220

The total energies of 256-atom supercells, $E^{\text{Mn}\uparrow\text{-Mn}\uparrow}$, $E^{\text{Mn}\uparrow\text{-Mn}\downarrow}$, E^{Mn} , and E^{Cu} have been calculated with the PAW method (calculation details are given in section II A) for the lattice spacing of 3.6792 Å, as has already been mentioned. These results, together with the SGPM

interaction at the first coordination shell obtained for the same lattice spacing in the dilute limit of Mn, are presented in Table I. As one can see, the agreement between the SGPM and PAW total-energy calculations for the nearest-neighbor effective pair interaction is very good. Below, we come back once more to the accuracy of the SGPM interactions used in the present statistical thermodynamic simulations.

B. Strain-induced interactions

To take the effect of local lattice relaxations into account, we have calculated strain-induced interactions at the first three coordination shells using Eq. (2), as described in Section II A. The interactions have been calculated in the dilute limit using the same 108- and 256-atom supercells as in the previous subsection. The results are presented in Table II together with the strain-induced interactions obtained by the Krivoglaz-Khachaturyan (KK) method^{48,49,50} using the experimental value for the lattice concentration expansion, $u = \frac{1}{a} \frac{da}{dc} = 0.0883$, for the $\text{Cu}_{0.83}\text{Mn}_{0.17}$ random alloy. One can see that the KK method, as it is implemented in Ref. 50, quite significantly overestimates the interactions especially at the third and fourth coordination shells. Therefore, in the calculations of the total effective pair interactions we have restricted ourselves only by inclusion the strain-induced interactions obtained in the first-principles calculations. Thus, we assume that the contribution from more distant strain-induced interactions to the configuration energetics is insignificant. Let us note that the long-range tail of the strain-induced interactions given by the KK model should be overestimated because it is valid only in the dilute limit. In random alloys, on the other hand, the long-range tail of strain-induced interactions should actually be damped by fluctuations of local lattice displacements due to the corresponding fluctuations of the local chemical environment of individual atoms.

Unfortunately, there exist no reliable way of getting distant strain-induced interactions in a random alloy from *ab initio* calculations. Nevertheless, strain-induced interactions are actually directly connected to the corresponding static lattice displacements within the Krivoglaz-Khachaturyan formalism. Thus, static lattice displacements in random alloys carry important information about strain-induced interactions. To investigate static displacements in the alloy, we have used the PAW method to calculate the relaxed atomic positions in a 108-atom supercell containing 90 Cu and 18 Mn atoms (corresponding to

TABLE II: Strain-induced interactions (in mRy) obtained from the Krivoglaz-Khachaturyan (KK) formalism and directly from supercell calculations. "CS" stands for the coordination shell number, also given by α . The parameters $V_{\alpha}^{\text{si, KK}}$ are obtained according to the procedure described in Ref. 50; V_{α}^{si} are calculated using Eq. (2).

CS, α	$V_{\alpha}^{\text{si, KK}}$	V_{α}^{si}	
		108-atom supercell	256-atom supercell
1	-2.151	-0.992	-1.176
2	-0.605	-0.100	
3	0.658	-0.166	
4	0.274		
5	-0.166		
6	0.034		
7	0.034		
8	-0.074		
9	0.091		
10	-0.063		

16.7 at %). The chemical and magnetic configurations have been set up in such a way as to minimize the short-range order parameters of the ternary alloy $\text{Mn}^{\uparrow}\text{-Mn}^{\downarrow}\text{-Cu}$. A static displacement for a given coordination shell has been obtained as an average over a symmetry group corresponding to the coordination shell.

The calculated atomic displacements $\langle \bar{x}_{lmn} \rangle$ are presented in Table III, where they are compared to the recent experimental data by Schönfeld *et al.*²¹ for $\text{Cu}_{0.83}\text{Mn}_{0.17}$. We also show the results for $\langle \bar{x}_{lmn}^{\text{CuMn}} \rangle$, $\langle \bar{x}_{lmn}^{\text{CuCu}} \rangle$, and $\langle \bar{x}_{lmn}^{\text{MnMn}} \rangle$ obtained from the supercell calculations of a single Mn (256-atom supercell) and a pair of Mn atoms (108-atom supercell), respectively. One can see that although there is a reasonable qualitative agreement between all the calculated results and experimental data, the quantitative differences in some cases are quite large. In particular, the theory and experiment predict different signs for the atomic displacements of Mn atoms in some cases. One can also note that Cu-Mn atomic displacements calculated for the alloy supercell and for the Mn impurity are quite different. Besides,

in case of impurity they decay much slower than in case of alloy.

TABLE III: Static displacements (multiplied by 10^3 for clarity) in units of the lattice constant obtained from our supercell calculations and taken from the experimental study where Georgopoulos-Cohen (GC) and 3λ separation methods were used (see Ref. 21 for details). The results of the calculations for Mn impurity and a pair of Mn atoms at the first three coordination shells for the values of $\langle \bar{x}_{lmn}^{\text{CuMn}} \rangle$, and $\langle \bar{x}_{lmn}^{\text{MnMn}} \rangle$, respectively, are given in parentheses.

lmn	Supercell calculations			Experiment ²¹					
	$\langle \bar{x}_{lmn}^{\text{CuCu}} \rangle$	$\langle \bar{x}_{lmn}^{\text{MnMn}} \rangle$	$\langle \bar{x}_{lmn}^{\text{CuMn}} \rangle$	$\langle x_{lmn}^{\text{CuCu}} \rangle$		$\langle x_{lmn}^{\text{MnMn}} \rangle$		$\langle x_{lmn}^{\text{CuMn}} \rangle$	
				GC	3λ	GC	3λ	GC	3λ
110	-0.78	-12.17 (-19.03)	3.84 (4.17)	-2.57	-2.32	-39.22	-31.81	7.20	7.20
200	1.03	-3.37 (-8.06)	-2.05 (-0.39)	1.70	1.56	2.73	9.20	-5.07	-5.55
211	-0.16	5.33 (2.20)	0.83 (1.87)	-0.07	-0.12	0.137	0.21	-0.01	0.26
121	-0.27	-2.32 (2.83)	0.53 (1.27)	-0.10	-0.76	0.9	-0.21	0.14	1.94
220	-0.57	4.02	0.83 (2.61)	-0.83	-0.70	-11.82	-6.07	2.82	2.10

We would like to note that such a comparison should be made with caution because the magnetic states in all these cases are different: the experiment is done in the paramagnetic state, the impurity calculations effectively produce results for the ferromagnetic state, and the alloy supercell calculations are performed in a kind of a "quasi-random" magnetic state. The latter may represent the DLM (paramagnetic) state only if the proper averaging over all possible magnetic configurations is performed. In a single calculation, any pair of Mn atoms is either ferromagnetically or antiferromagnetically aligned rather than being in an average DLM state. In our view, a quite broad spectrum of the results for static atomic displacements reflects the complexity of the problem that requires further investigation.

IV. ATOMIC CONFIGURATION OF $\text{Cu}_{0.83}\text{Mn}_{0.17}$ ALLOY

The atomic configuration of the $\text{Cu}_{0.83}\text{Mn}_{0.17}$ alloy has been obtained in Monte Carlo calculations using the Metropolis algorithm in the canonical ensemble based on the Hamiltonian (1) at 500 K, which is the annealing temperature in the diffuse scattering experiments described in Ref. 8. Simulation boxes of different sizes (up to $32 \times 32 \times 32$ fcc elementary

cubic cells) have been taken to exclude finite-size effects. A run has consisted of 15000 sweeps, with 10000 sweeps used for collecting statistics. The short-range order parameters have been determined up to the 80th coordination shell; their Fourier transform is presented in Fig. 4 along with the experimental data from Ref. 8. Clearly, the ASRO is reproduced very well up to the width of the peaks. A slight difference in the shape can be either due to a small error originating from the cut-off of the interaction range, and multi-site terms for more than 4 sites, or due to an incomplete subtraction of the magnetic contribution from neutron-scattering intensity data. The latter claim is supported by subtracting the calculated normalized atomic intensity pattern from the experimental one and noting that their difference matches the magnetic intensity pattern quite well.

The ASRO in the $\text{Cu}_{0.83}\text{Mn}_{0.17}$ alloy is characterized by $Q_a = (1, 1/2, 0)$ type of atomic ordering. The local maximum of the Fourier transform of the SRO parameters at $(0, 0, 0)$ is also present, yet it is very weak, implying a strong tendency toward ordering rather than segregation. There has been a controversy as to what kind of an ordered phase this ASRO represents.^{19,51,52,53} None of the previously proposed ordered structures (e.g., DO_{22} , A_2B_2 , $D1_a$, etc.) satisfies all the necessary conditions, such as the absence of additional reflections at points inequivalent to Q_a (such as for DO_{22}) or the abundance of Cu in the ordered precipitates (this disfavors A_2B_2). To find the sought-for ordered structure, we have performed Monte Carlo simulations down to low temperatures. Below the transition temperature ($T_c \approx 250\text{K}$), an ordered phase with 25 at% Mn has precipitated. The structure of the phase (first proposed in Ref. 54 as an ordered phase for the Ni_3Mo alloy) is shown in Fig. 5. It consists of stripes similar to the A_2B_2 structure, but with half of the Mn stripes being replaced by Cu.

It is worth noting, however, that the ordering energy of the obtained Cu_3Mn phase (referred to as DO_{60} hereafter) is very close to that of the $D1_a$ (Ni_4Mo) phase. It turns out that three-site chemical interactions play a crucial role in stabilizing the DO_{60} structure. Unfortunately, there is no simple way to check the stability of the Cu_3Mn and Cu_4Mn phases with respect to each other, since this would require calculating the free energy for the alloy at different concentrations, which is a formidable task due to a strong effect of magnetism on the alloy thermodynamics.

The ordering energies of the obtained DO_{60} phase, as well as the energies of some other ordered structures for the same composition, have been calculated and compared to direct

TABLE IV: Ordering energies of different Cu_3Mn structures: E_{tot} are calculated as the difference between the total energy of an ordered phase and a random alloy, with the Mn atoms being in the DLM state; E_{SGPM} are obtained from the effective interactions $V^{(m)}$ ($m = 2, 3, 4$).

Structure	E_{SGPM} (mRy)	E_{tot} (mRy)	$E_{\text{SGPM}} - E_{\text{SGPM}}^{DO_{60}}$ (mRy)	$E_{\text{tot}} - E_{\text{tot}}^{DO_{60}}$ (mRy)
L_{12}	1.68	2.6	2.51	2.89
DO_{22}	-0.83	0.26	0.54	0.54
DO_{60}	-1.68	-0.29	0.0	0.0

total-energy calculations performed with the EMTO method. The results are presented in Table IV. It is obvious that among the other Cu_3Mn phases, the DO_{60} phase is the most stable one at the given composition, and the energy difference with respect to the DO_{22} structure ensures that minor corrections (static displacements, phonon contribution, etc.) cannot change the observed behavior.

V. MAGNETIC STRUCTURE

As a rule, accurate numerical studies of SG systems by Monte Carlo methods are computationally very demanding. However, a general picture of magnetic correlations turns out to be relatively insensitive to the quality of sampling. We have employed the Metropolis algorithm for the Hiesenberg Monte Carlo simulations to obtain pair spin-spin correlations in the temperature range between 300 and 20K. The atomic configurations have been obtained in the Ising atomic Monte Carlo simulations at 500 K and kept fixed during magnetic simulations because the atomic diffusion is practically absent at ambient and lower temperatures.

Despite frustration that impedes equilibration in simulations even above the SG transition temperature, the spin-spin correlations tend to saturate to their equilibrium values much faster than quantities characterizing the SG phase. To put this another way, the autocorrelation time associated with the spin-spin correlations changes smoothly and remains relatively small down to the lowest temperatures owing to the absence of the second-order transition. We can thus make do with a simplified Monte Carlo technique to achieve a reasonable accuracy with a moderate number of time steps in this case.

To characterize a MSRO, a spin-spin correlation function $C(R) = \frac{1}{N} \sum_i \langle \vec{S}_i \vec{S}_{i+R} \rangle$ has been calculated. The Fourier transform of the spin-spin correlation function obtained from the simulations at 20K is presented in Fig. 6 along with the experimental data on the corresponding polarized neutron-scattering intensities. The maxima at $Q_s = (1, 1/2 \pm \delta, 0)$ ($\delta \approx 0.21$ for $c_{\text{Mn}} = 0.172$) correspond to incommensurate SDW clusters. It has already been contemplated⁵¹ that the local magnetic order represents a non-collinear single- Q spin-spiral structure, with the directions of propagation of SDWs varying in different domains. This type of the local magnetic order is observed in simulations at low temperatures (20K). Since the correlations at the first several coordination shells are strong, these clusters, rather than individual spins, determine the spin dynamics close to the freezing temperature T_{SG} . Also, non-collinear MSRO clusters may be responsible for the chirality ordering that accompanies the SG transition.⁵⁵

It is worth noting that we neglect anisotropy for the pure $\text{Cu}_{0.83}\text{Mn}_{0.17}$ alloy because the anisotropy energy for this alloy is too small (of the order of 10^{-3} meV per Mn atom⁵⁶) to have any considerable effect on the MSRO. A situation, however, can be different in CuMn alloys containing heavy impurities. For instance, adding even a small amount of Pt to the alloy results in the anisotropy energy of up to 0.1 meV per Mn atom.^{57,58}

VI. SPIN-GLASS BEHAVIOR

In simulating a SG system, one has to take into account the fact that most of the quantities specific to a SG state, such as SG susceptibility, overlap parameters, etc., are quite sensitive to a realization of disorder² and a configurational averaging must therefore be carried out. The latter requires a large number of independent runs. Moreover, to obtain unbiased values of ensemble averages for each configuration, it is important to have samples in the equilibrium state. However, due to magnetic frustrations in the alloy it is hard to achieve the equilibration, and improved methods must be employed to get results on a reasonable time scale.

Slow equilibration imposes a restriction on a system size in simulations and therefore finite-size effects become an important issue. To overcome the size and boundary dependences, we resort to a technique that has become a standard tool in investigations of critical phenomena, namely, the finite-size scaling procedure.^{59,60} The general idea is to obtain a

dimensionless correlation length, ξ/L , for different system linear sizes, L (defined in terms of the number of elementary cubic cells of the fcc lattice), and use the scaling law

$$\xi_L/L = f(L^{1/\nu}(T - T_c)), \quad (8)$$

to determine a transition temperature T_c by taking advantage of a simple corollary of the fact that the dimensionless correlation length becomes independent of L at T_c . To calculate the correlation length, two independent replicas with identical atomic distributions have been simulated in parallel and the correlation length has been evaluated according to the following well-known formula:⁶¹

$$\xi_L = \frac{1}{2 \sin(k_{\min}^x/2)} \sqrt{\frac{\chi_{\text{SG}}(\mathbf{0})}{\chi_{\text{SG}}(\mathbf{k}_{\min})} - 1}, \quad (9)$$

where $\mathbf{k}_{\min} = 2\pi/L(1, 0, 0)$ and the SG correlation function $\chi_{\text{SG}}(\mathbf{k})$ is defined as

$$\chi_{\text{SG}}(\mathbf{k}) = N \left[\sum_{\mu\nu} \langle |q^{\mu\nu}(\mathbf{k})|^2 \rangle \right]_{\text{av}}, \quad (10)$$

$$q^{\mu\nu}(\mathbf{k}) = \frac{1}{N} \sum_i S_i^{\mu(1)} S_i^{\nu(2)} e^{i\mathbf{k}\mathbf{R}_i}, \quad (11)$$

with indices (1) and (2) designating quantities related to the two replicas; summations are performed over all magnetic atoms in the alloy, $\langle \dots \rangle$ and $[\dots]_{\text{av}}$ stand for thermal and configurational averaging, respectively, and $N = 4L^3$. The FSS scaling of the SG susceptibility $\chi_{\text{SG}} \equiv \chi_{\text{SG}}(\mathbf{0})$ is given by the relation

$$\chi_{\text{SG}}/L^{2-\eta} = X(L^{1/\nu}(T - T_c)). \quad (12)$$

Monte Carlo simulations have been performed using the heat-bath algorithm.⁶² To make calculations practically affordable, only the exchange interaction parameters with $|\mathbf{R}_{ij}| < r_0 = 4$ elementary cubic cells have been taken into account. To ensure thermalization, logarithmic binning has been applied to the spin-glass susceptibility $\chi_{\text{SG}}(0)$ and a consistency check of the obtained configurational averages has been made in a way similar to that in Ref. 63, namely, the following two quantities have been calculated:

$$\chi_o = \frac{1}{N} \left[\sum_i \langle \mathbf{S}_i^{(1)} \cdot \mathbf{S}_i^{(2)} \rangle^2 \right]_{\text{av}} \quad (13)$$

and

$$\chi_d = \frac{1}{T} \sum_t \left[\frac{1}{N} \left(\sum_i \mathbf{S}_i^{(1)}(t_0) \cdot \mathbf{S}_i^{(1)}(t_0 + t) \right)^2 \right]_{\text{av}}, \quad (14)$$

where t designates the time in terms of Monte Carlo steps, t_0 is the equilibration time, and T the size of the time window during which measurements are carried out. A calculation is considered converged with respect to the configurational averaging if a condition $\chi_o = \chi_d$ is satisfied with a high accuracy (to within 1%). To accelerate equilibration, we have used the overrelaxation method,⁶⁴ which consists in performing microcanonical steps; that is, all spins are flipped sequentially according to the following energy-conserving transformation:

$$\mathbf{S}_i \rightarrow \mathbf{S}_i - \frac{2 \left(\mathbf{S}_i \cdot \frac{\partial H}{\partial \mathbf{S}_i} \right) \frac{\partial H}{\partial \mathbf{S}_i}}{\left(\frac{\partial H}{\partial \mathbf{S}_i} \right)^2}. \quad (15)$$

L sequential microcanonical steps for each heat-bath sweep have been found to be optimal in terms of the actual calculation time.

The calculated size dependence of the SG susceptibility (Fig. 7) suggests the divergent behavior below 100K. More detailed information can be extracted from the size scaling of the dependence of the correlation length on temperature (Fig. 8). The results show unequivocally that the system undergoes a transition at a finite temperature. The absence of a long-range order has been checked by observing the development of the correlation length corresponding to the SDW ordering. Although the SG transition is clearly observed, one cannot rule out a crossover to a marginal behavior at larger supercell sizes. The data exhibit a universal scaling with $T_c = 57 \pm 5K$ and $\nu = 0.95 \pm 0.1$ (Fig. 9). Using these parameters, the SG susceptibility can also be fitted providing a parameter $\eta = 0.25 \pm 0.1$ (Fig. 10). From the relation $\gamma = \nu(2 - \eta)$, one can also find that $\gamma \approx 1.7 \pm 0.3$. In all plots, the deviation of the data for $L = 16$ is due to the systematic underestimation of the SG susceptibility at low temperatures.

An alternative (extended) scaling relation based on the high-temperature series expansion was proposed by Campbell *et al.*⁶⁵ Unlike the conventional scaling [Eq. (8)], the extended scaling applies not only to a close vicinity of the critical region but must also hold for all temperatures above the transition. The extended relation, that can be written as⁶⁵

$$\xi_L/L = \tilde{f} \left((LT)^{1/\nu} [1 - (T_c/T)^2] \right), \quad (16)$$

$$\chi_{SG}/(LT)^{2-\eta} = \tilde{X} \left((LT)^{1/\nu} [1 - (T_c/T)^2] \right), \quad (17)$$

has been applied to the calculated data. The results shown in Figs. 11 and 12 demonstrate a rather good scaling, although a larger temperature interval and higher accuracy are required to make a more thorough comparison of the two types of scalings.

The values of the critical exponents differ from those obtained in experimental measurements²⁵ from which we have $\nu_{exp} = 1.3 \pm 0.15$ and $\gamma_{exp} = 2.3 \pm 0.2$. One of the possible causes of this disagreement is a rather high sensitivity of the critical exponents to the scaling corrections which might be non-negligible in our calculations because the range of the interactions is comparable to the size of the simulation box. Another effect, which can strongly influence the critical behavior, is anisotropy. It is well known that even a small amount of anisotropy present in a real system can change the critical behavior close to the transition temperature, giving rise to the values of critical exponents different from those for an isotropic system. Unfortunately, it is practically impossible to detect any crossover from an isotropic to anisotropic critical behavior in small systems such as the one we have used here and with such a small anisotropy energy typical for pure CuMn alloys. Simulations for systems with an appreciable amount of anisotropy (such as, e.g., CuMn_xPt_y) can therefore be an interesting problem for future work.

The obtained transition temperature, 57K, turns out to be slightly lower than the experimental value (78K). One of the possible explanations for this discrepancy is the cut-off of the interaction range that we had to introduce. On the other hand, Monte Carlo dynamics (only local updates without overrelaxation) has revealed a strong critical slowing down at about a temperature equal to 80K, and this value only slightly depends on the cut-off. This could indicate that while dynamics is driven primarily by short-range interactions, the SG transition itself is very sensitive to long-range interactions which may play a rather important role in the onset of the SG phase in the CuMn alloys.

In spite of a possible strong influence of long-range interactions on the SG dynamics, it seems unlikely that the dominating contribution to the onset of the transition comes from effectively infinite-range interactions because a natural cut-off can be considered originating from various kinds of imperfections (vacancies, impurities, static displacements, etc.) present in any real material but discarded in the current study. For instance, we have neglected static atomic displacements in the magnetic part of the problem. Although their effect should be very small on the effective interactions at nearest-neighbor interactions, more distant interaction will be definitely damped because of the corresponding exponential damping

of the Cu s -like states. This means that such a system will doubtfully cross over to a mean-field-like transition in a realistic model.

VII. CONCLUDING REMARKS

The basic result of this work is the structure of the CuMn alloy obtained from first-principles calculations. It has been shown that both the atomic and magnetic thermodynamics simulations accurately reproduce the corresponding experimental data. Interestingly, it has already been pointed out in some studies¹⁹ that the most probable stoichiometry of the ordered phase of a Cu-rich CuMn alloy is Cu-25 at% Mn; however, the scattering pattern of known structures with this composition (DO_{22} , L_{12}) is not compatible with the observed one, and the A_2B_2 structure, that lacks this drawback, has been considered as a best description of the ASRO. In this respect, the structure DO_{60} , on one hand, contains 25 at% Mn and, on the other hand, resembles the A_2B_2 structure closely and produces a similar scattering intensity picture with the dominant peaks at $Q_a = (1, 1/2, 0)$. This reconciles a seeming discrepancy between the observed stoichiometry and the structure of the ASRO.

In spite of some limitations of the approach used, a large class of metallic spin-glass materials, e.g., AgMn, AuMn, PtMn, AuFe, etc., can be investigated in a similar fashion. Other contributions to the magnetic interactions might be required to be taken into consideration, though. Although in the CuMn alloy relativistic effects can be neglected, in systems with heavy elements (Au, Pt) they are important and can lead to strongly anisotropic interactions. Most of the anisotropic contributions can be treated within the GPM formalism in the framework of a fully relativistic code (see, e.g., Ref. 66), extending thus the approach to highly anisotropic heavy-element metallic alloys.

Acknowledgments

We are grateful to the Swedish Research Council (VR) and the Swedish Foundation for Strategic Research (SSF) for financial support. Calculations were done using UPPMAX (Uppsala) and NSC (Linköping) resources.

APPENDIX

Effective cluster interactions for two-site, three-site and four-site clusters are presented in Tables V-VII. In all cases, an m -site cluster is represented by the first atom at the origin, $(0,0,0)$, and $(m-1)$ vectors corresponding to the other atoms in the cluster as given in the tables. The interactions are given in millirydberg (mRy). Note that the accuracy of the EMTO calculations has been set to 10^{-3} mRy.

-
- ¹ V. Cannella and J. A. Mydosh, Phys. Rev. B **6**, 4220 (1972).
² K. Binder and A. P. Young, Rev. Mod. Phys. **58**, 801 (1986).
³ S. F. Edwards and P. W. Anderson, J. Phys. F: Met. Phys. **5**, 965 (1975).
⁴ J. W. Cable, S. A. Werner, G. P. Felcher, and N. Wakabayashi, Phys. Rev. Lett. **49**, 829 (1982).
⁵ J. W. Cable and Y. Tsunoda, J. Appl. Phys. **73**, 5454 (1993).
⁶ J. R. Davis, S. K. Burke, and B. D. Rainford, J. Magn. Magn. Mater. **15-18**, 151 (1980).
⁷ F. J. Lamelas, S. A. Werner, S. M. Shapiro, and J. A. Mydosh, Phys. Rev. B **51**, 621 (1995).
⁸ B. Schönfeld, R. Bucher, G. Kostorz, and M. Zolliker, Phys. Rev. B **69**, 224205 (pages 9) (2004).
⁹ Y. Tsunoda, N. Kunitomi, and J. W. Cable, J. Appl. Phys. **57**, 3753 (1985).
¹⁰ P. Wells and J. H. Smith, J. Phys. F: Met. Phys. **1**, 763 (1971).
¹¹ S. A. Werner, J. J. Rhyne, and J. A. Gotaas, Solid State Commun. **56**, 457 (1985).
¹² D. L. Martin, Phys. Rev. B **21**, 1902 (1980).
¹³ A. P. Murani and A. Heidemann, Phys. Rev. Lett. **41**, 1402 (1978).
¹⁴ E. M. Gray, T. J. Hicks, and J. H. Smith, J. Phys. F: Met. Phys. **12**, L189 (1982).
¹⁵ T. M. Harders, T. J. Hicks, and J. H. Smith, J. Phys. F: Met. Phys. **13**, 1263 (1983).
¹⁶ T. M. Harders and P. Wells, J. Phys. F: Met. Phys. **13**, 1017 (1983).
¹⁷ L. Lundgren, P. Svedlindh, P. Nordblad, and O. Beckman, Phys. Rev. Lett. **51**, 911 (1983).
¹⁸ F. Mezei, J. Appl. Phys. **53**, 7654 (1982).
¹⁹ J. W. Cable, S. A. Werner, G. P. Felcher, and N. Wakabayashi, Phys. Rev. B **29**, 1268 (1984).
²⁰ H. Roelofs, B. Schönfeld, G. Kostorz, W. Bührer, J. L. Robertson, P. Zschack, and G. E. Ice, Scripta Mater. **34**, 1393 (1996).
²¹ B. Schönfeld, H. Roelofs, G. Kostorz, J. L. Robertson, P. Zschack, and G. E. Ice, Phys. Rev. B

- 77**, 144202 (pages 8) (2008).
- ²² S. Nagata, P. H. Keesom, and H. R. Harrison, Phys. Rev. B **19**, 1633 (1979).
 - ²³ R. W. Knitter, J. S. Kouvel, and H. Claus, J. Magn. Magn. Mater. **5**, 356 (1977).
 - ²⁴ C. A. M. Mulder, A. J. van Duynveldt, and J. A. Mydosh, Phys. Rev. B **23**, 1384 (1981).
 - ²⁵ L. P. Lévy, Phys. Rev. B **38**, 4963 (1988).
 - ²⁶ A. Oswald, R. Zeller, P. J. Braspenning, and P. H. Dederichs, J. Phys. F: Met. Phys. **15**, 193 (1985).
 - ²⁷ M. F. Ling, J. B. Staunton, and D. D. Johnson, J. Phys.: Condens. Matter **6**, 6001 (1994).
 - ²⁸ M. Ling, J. Staunton, D. Johnson, and F. Pinski, J. Magn. Magn. Mater. **177-181**, 1399 (1998).
 - ²⁹ B. L. Györfy and G. M. Stocks, Phys. Rev. Lett. **50**, 374 (1983).
 - ³⁰ A. V. Ruban, P. A. Korzhavyi, and B. Johansson, Phys. Rev. B **77**, 094436 (pages 5) (2008).
 - ³¹ E. M. Gray, J. Phys.: Condens. Matter **8**, 751 (1996).
 - ³² A. V. Ruban, S. Shallcross, S. I. Simak, and H. L. Skriver, Phys. Rev. B **70**, 125115 (pages 19) (2004).
 - ³³ L. Vitos, Phys. Rev. B **64**, 014107 (2001).
 - ³⁴ L. Vitos, I. A. Abrikosov, and B. Johansson, Phys. Rev. Lett. **87**, 156401 (2001).
 - ³⁵ B. L. Györfy, A. J. Pindor, J. Staunton, J. M. Stocks, and H. Winter, J. Phys. F: Met. Phys. **15**, 1337 (1985).
 - ³⁶ A. V. Ruban and H. L. Skriver, Phys. Rev. B **66**, 024201 (2002).
 - ³⁷ A. V. Ruban, S. I. Simak, P. A. Korzhavyi, and H. L. Skriver, Phys. Rev. B **66**, 024202 (2002).
 - ³⁸ I. A. Abrikosov, S. I. Simak, B. Johansson, A. V. Ruban, and H. L. Skriver, Phys. Rev. B **56**, 9319 (1997).
 - ³⁹ N. Cowlam, G. E. Bacon, and L. Gillott, J. Phys. F: Met. Phys. **7**, L315 (1977).
 - ⁴⁰ G. Kresse and D. Joubert, Phys. Rev. B **59**, 1758 (1999).
 - ⁴¹ P. E. Blöchl, Phys. Rev. B **50**, 17953 (1994).
 - ⁴² W. Kohn and L. J. Sham, Phys. Rev. **140**, A1133 (1965).
 - ⁴³ J. P. Perdew and Y. Wang, Phys. Rev. B **45**, 13244 (1992).
 - ⁴⁴ G. Kresse and J. Hafner, Phys. Rev. B **48**, 13115 (1993).
 - ⁴⁵ G. Kresse and J. Furthmüller, Comp. Mater. Sci. **6**, 15 (1996).
 - ⁴⁶ G. Kresse and J. Furthmüller, Phys. Rev. B **54**, 11169 (1996).
 - ⁴⁷ A. I. Liechtenstein, M. I. Katsnelson, V. P. Antropov, and V. A. Gubanov, J. Magn. Magn.

- Mater. **67**, 65 (1987).
- ⁴⁸ M. A. Krivoglaz, *X-ray and neutron diffraction in nonideal crystals* (Springer, Berlin, 1995).
 - ⁴⁹ A. G. Khachaturyan, *Theory of structural transformations in solids* (Wiley, New York, 1983).
 - ⁵⁰ M. S. Blanter, phys. stat. sol. (b) **181**, 377 (1994).
 - ⁵¹ Y. Tsunoda and J. W. Cable, Phys. Rev. B **46**, 930 (1992).
 - ⁵² M. Hirabayashi, M. Koiwa, S. Yamaguchi, and K. Kamata, J. Phys. Soc. Jpn. **45**, 1591 (1978).
 - ⁵³ H. Bouchiat, E. Dartyge, P. Monod, and M. Lambert, Phys. Rev. B **23**, 1375 (1981).
 - ⁵⁴ U. D. Kulkarni and S. Banerjee, Acta Metall. **36**, 413 (1988).
 - ⁵⁵ H. Kawamura, Phys. Rev. Lett. **68**, 3785 (1992).
 - ⁵⁶ J. Kouvel, J. Phys. Chem. Solids **21**, 57 (1961).
 - ⁵⁷ A. Fert and P. M. Levy, Phys. Rev. Lett. **44**, 1538 (1980).
 - ⁵⁸ J. J. Préjean, M. Joliclerc, and P. Monod, J. Phys. (Paris) **41**, 427 (1980).
 - ⁵⁹ M. N. Barber, *Phase Transitions and Critical Phenomena*, vol. 9 (Academic, New York, 1984).
 - ⁶⁰ D. P. Landau and K. Binder, *A Guide to Monte Carlo Simulations in Statistical Physics* (Cambridge University Press, 2000).
 - ⁶¹ L. W. Lee and A. P. Young, Phys. Rev. Lett. **90**, 227203 (2003).
 - ⁶² J. A. Olive, A. P. Young, and D. Sherrington, Phys. Rev. B **34**, 6341 (1986).
 - ⁶³ R. N. Bhatt and A. P. Young, Phys. Rev. Lett. **54**, 924 (1985).
 - ⁶⁴ I. Campos, M. Cotallo-Aban, V. Martin-Mayor, S. Perez-Gaviro, and A. Tarancon, Phys. Rev. Lett. **97**, 217204 (2006).
 - ⁶⁵ I. A. Campbell, K. Hukushima, and H. Takayama, Phys. Rev. Lett. **97**, 117202 (2006).
 - ⁶⁶ L. V. Pourovskii, A. V. Ruban, L. Vitos, H. Ebert, B. Johansson, and I. A. Abrikosov, Phys. Rev. B **71**, 094415 (2005).

FIG. 1: (Color online) Chemical and total (chemical and strain-induced) interactions for the first 20 coordination shells. $V^{(2)}$ and $V^{(2),\text{bare}}$ are the chemical interactions with and without (bare) the screening contribution. The total pair interaction in the disordered phase is given by the sum $V^{(2)} + V^{\text{si}}$.

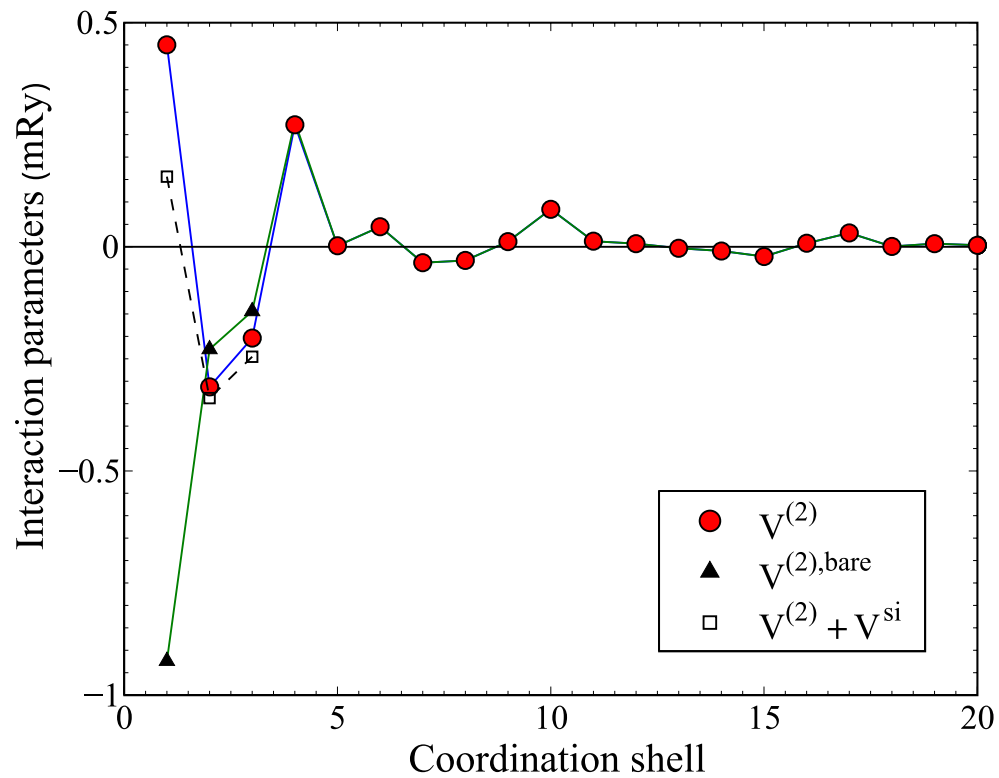


TABLE V: Pair effective and magnetic exchange interactions for the first 80 coordination spheres.

N	(R_x, R_y, R_z)	$V_{(R_0, R)}^{(2)}$	$J_{(R_0, R)}^{(xc)}$	N	(R_x, R_y, R_z)	$V_{(R_0, R)}^{(2)}$	$J_{(R_0, R)}^{(xc)}$
1	(0.5, 0.5, 0.0)	0.45035	-2.51559	41	(2.5, 2.5, 2.0)	0.00003	-0.00029
2	(1.0, 0.0, 0.0)	-0.31257	0.83820	42	(3.5, 2.0, 0.5)	0.00358	-0.00001
3	(1.0, 0.5, 0.5)	-0.20378	0.18558	43	(4.0, 0.5, 0.5)	0.00030	0.00003
4	(1.0, 1.0, 0.0)	0.27218	-0.29230	44	(4.0, 1.0, 0.0)	0.00038	-0.00118
5	(1.5, 0.5, 0.0)	0.00205	-0.05987	45	(3.0, 2.0, 2.0)	0.00143	-0.00052
6	(1.0, 1.0, 1.0)	0.04462	-0.00211	46	(3.0, 2.5, 1.5)	-0.00003	0.00016
7	(1.5, 1.0, 0.5)	-0.03562	0.06212	47	(3.0, 3.0, 0.0)	0.00358	-0.01198
8	(2.0, 0.0, 0.0)	-0.03068	0.07661	48	(4.0, 1.0, 1.0)	-0.00122	-0.00056
9	(2.0, 0.5, 0.5)	0.01150	0.00673	49	(3.5, 2.0, 1.5)	-0.00050	-0.00105
10	(1.5, 1.5, 0.0)	0.08350	-0.06621	50	(4.0, 1.5, 0.5)	-0.00057	-0.00273
11	(2.0, 1.0, 0.0)	0.01215	-0.07616	51	(3.5, 2.5, 0.0)	-0.00095	-0.01165
12	(1.5, 1.5, 1.0)	0.00675	-0.01083	52	(3.0, 3.0, 1.0)	0.00082	-0.00236
13	(2.0, 1.0, 1.0)	-0.00328	0.01124	53	(3.5, 2.5, 1.0)	-0.00052	-0.00147
14	(2.5, 0.5, 0.0)	-0.00948	0.01708	54	(4.0, 2.0, 0.0)	-0.00358	0.00909
15	(2.0, 1.5, 0.5)	-0.02198	0.04217	55	(4.5, 0.5, 0.0)	0.00025	-0.00078
16	(2.5, 1.0, 0.5)	0.00750	-0.00194	56	(4.0, 1.5, 1.5)	0.00093	0.00150
17	(2.0, 2.0, 0.0)	0.03080	-0.03656	57	(4.0, 2.0, 1.0)	0.00042	0.00171
18	(2.0, 1.5, 1.5)	0.00063	-0.00303	58	(3.5, 3.0, 0.5)	0.00032	0.00660
19	(2.5, 1.5, 0.0)	0.00688	-0.04823	59	(4.5, 1.0, 0.5)	-0.00093	0.00041
20	(2.0, 2.0, 1.0)	0.00328	-0.00889	60	(3.0, 2.5, 2.5)	-0.00005	0.00002
21	(3.0, 0.0, 0.0)	0.00585	-0.00193	61	(3.0, 3.0, 2.0)	-0.00003	0.00006
22	(3.0, 0.5, 0.5)	-0.00287	-0.00186	62	(3.5, 2.5, 2.0)	0.00232	0.00016
23	(2.5, 1.5, 1.0)	-0.00118	0.00076	63	(4.0, 2.5, 0.5)	0.00003	-0.00114
24	(3.0, 1.0, 0.0)	-0.00775	0.01594	64	(4.5, 1.5, 0.0)	0.00103	-0.00023
25	(2.5, 2.0, 0.5)	-0.00937	0.02320	65	(4.5, 1.5, 1.0)	-0.00047	-0.00164
26	(3.0, 1.0, 1.0)	0.00363	-0.00354	66	(3.5, 3.0, 1.5)	-0.00003	0.00010
27	(3.0, 1.5, 0.5)	0.00617	-0.00055	67	(4.0, 2.0, 2.0)	-0.00010	-0.00125
28	(2.0, 2.0, 2.0)	0.00025	-0.00037	68	(4.0, 2.5, 1.5)	0.00068	-0.00028
29	(2.5, 2.0, 1.5)	0.00065	-0.00097	69	(3.5, 3.5, 0.0)	-0.00057	-0.00557
30	(2.5, 2.5, 0.0)	0.01150	-0.02220	70	(4.5, 2.0, 0.5)	-0.00015	-0.00206
31	(3.5, 0.5, 0.0)	0.00093	0.00056	71	(4.0, 3.0, 0.0)	-0.00118	-0.00410
32	(3.0, 2.0, 0.0)	0.00150	-0.02508	72	(5.0, 0.0, 0.0)	0.00028	-0.00067
33	(3.5, 1.0, 0.5)	0.00220	-0.00129	73	(5.0, 0.5, 0.5)	0.00028	-0.00019
34	(2.5, 2.5, 1.0)	-0.00178	-0.00397	74	(3.5, 3.5, 1.0)	0.00003	-0.00118
35	(3.0, 1.5, 1.5)	-0.00155	0.00064	75	(4.0, 3.0, 1.0)	-0.00032	-0.00073
36	(3.0, 2.0, 1.0)	-0.00100	-0.00282	76	(5.0, 1.0, 0.0)	-0.00010	-0.00014
37	(3.5, 1.5, 0.0)	-0.00553	0.01155	77	(4.5, 2.5, 0.0)	0.00010	0.00669
38	(3.5, 1.5, 1.0)	-0.00343	0.00050	78	(4.5, 2.0, 1.5)	-0.00217	0.00167
39	(3.0, 2.5, 0.5)	0.00185	0.01314	79	(5.0, 1.0, 1.0)	0.00030	0.00041
40	(4.0, 0.0, 0.0)	0.00000	-0.00067	80	(3.0, 3.0, 3.0)	-0.00005	0.00010

TABLE VI: Selected three-site effective interactions. The corresponding three-site clusters are defined by three vectors: $R_0 \equiv (0,0,0)$, R_1 , R_2 .

N	R_1	R_2	$V_{(R_0,R_1,R_2)}^{(3)}$	N	R_1	R_2	$V_{(R_0,R_1,R_2)}^{(3)}$
1	(0.5, 0.0, 0.5)	(0.5, 0.5, 0.0)	-0.01127	15	(0.5, 0.5, 0.0)	(1.0, 1.5, 0.5)	0.00667
2	(0.5, 0.5, 0.0)	(1.0, 0.0, 0.0)	-0.02395	16	(0.5, 0.5, 0.0)	(1.5, 0.5, 1.0)	0.00561
3	(0.5, 0.5, 0.0)	(1.0, 0.5, 0.5)	0.04451	17	(0.5, 0.5, 0.0)	(-0.5, 1.0, 1.5)	0.00213
4	(0.5, 0.5, 0.0)	(0.5, 0.5, 1.0)	-0.00140	18	(1.0, 0.0, 0.0)	(1.5, 1.0, 0.5)	0.00135
5	(0.5, 0.5, 0.0)	(-0.5, 1.0, 0.5)	0.00470	19	(0.5, 0.5, 0.0)	(2.0, 0.0, 0.0)	0.00235
6	(1.0, 0.0, 0.0)	(0.5, 0.5, 1.0)	0.00125	20	(0.5, 0.5, 0.0)	(1.5, 1.5, 0.0)	-0.01867
7	(0.5, 0.5, 1.0)	(1.0, -0.5, 0.5)	-0.00014	21	(1.0, 1.0, 0.0)	(2.0, 2.0, 0.0)	-0.00609
8	(0.5, 0.5, 0.0)	(1.0, 1.0, 0.0)	-0.04427	22	(0.5, 0.5, 0.0)	(2.5, 2.5, 0.0)	-0.00231
9	(0.5, 0.5, 0.0)	(1.0, 0.0, 1.0)	-0.00305	23	(0.5, 0.5, 0.0)	(2.0, 2.0, 0.0)	-0.00724
10	(1.0, 0.0, 0.0)	(1.0, 1.0, 0.0)	-0.00303	24	(1.0, 1.0, 0.0)	(2.5, 2.5, 0.0)	-0.00230
11	(0.5, 0.5, 0.0)	(1.5, 0.0, 0.5)	-0.00210	25	(0.5, 0.5, 0.0)	(3.0, 3.0, 0.0)	-0.00055
12	(0.5, 0.5, 0.0)	(1.5, -0.5, 0.0)	-0.00181	26	(1.0, 1.0, 0.0)	(3.0, 3.0, 0.0)	-0.00077
13	(0.5, 0.5, 0.0)	(0.5, 0.0, 1.5)	-0.00324	27	(1.5, 1.5, 0.0)	(3.0, 3.0, 0.0)	-0.00088
14	(0.5, 0.5, 0.0)	(1.0, 1.0, 1.0)	-0.00687	28	(1.5, 1.5, 0.0)	(3.0, 3.0, 0.0)	0.00000

TABLE VII: Selected four-site effective interactions. The corresponding four-site clusters are defined by four vectors: $R_0 \equiv (0, 0, 0)$, R_1, R_2, R_3 .

N	R_1	R_2	R_3	$V_{(R_0, R_1, R_2, R_3)}^{(4)}$
1	(0.5, 0.5, 0.0)	(0.5, 0.0, 0.5)	(0.0, 0.5, 0.5)	0.00418
2	(0.5, -0.5, 0.0)	(0.5, 0.5, 0.0)	(0.5, 0.0, 0.5)	0.00459
3	(0.5, 0.5, 0.0)	(1.0, 0.0, 0.0)	(0.5, -0.5, 0.0)	0.00164
4	(0.5, 0.0, 0.5)	(1.0, 0.5, 0.5)	(0.5, 0.5, 0.0)	0.00003
5	(1.0, 0.0, 0.0)	(1.0, 0.5, 0.5)	(0.5, 0.5, 0.0)	-0.00113
6	(0.5, 0.5, 0.0)	(0.5, 1.0, 0.5)	(1.0, 0.5, 0.5)	0.00064
7	(0.5, 0.5, 0.0)	(1.0, 0.5, 0.5)	(1.0, 0.5, -0.5)	-0.00038
8	(0.5, 0.0, 0.5)	(0.5, 1.0, 0.5)	(1.0, 0.5, 0.5)	-0.00019
9	(0.5, 0.5, 0.0)	(1.0, 1.0, 0.0)	(1.0, 0.5, 0.5)	-0.00096
10	(0.5, 0.5, 0.0)	(1.0, 1.0, 0.0)	(1.5, 1.5, 0.0)	0.00120
11	(1.0, 0.0, 0.0)	(1.0, 0.5, 0.5)	(1.0, 0.5, -0.5)	0.00022
12	(0.0, 0.5, 0.5)	(0.5, 0.0, 0.5)	(-0.5, -0.5, 1.0)	-0.00043
13	(1.0, 0.0, 0.0)	(1.0, 0.5, 0.5)	(0.5, 1.0, 0.5)	-0.00005
14	(0.5, -0.5, 0.0)	(0.5, -0.5, -1.0)	(-0.5, -1.0, -0.5)	0.00005
15	(0.5, 0.5, 0.0)	(1.0, 1.0, 0.0)	(1.0, 0.0, 0.0)	0.00032

FIG. 2: (Color online) Concentration dependence of the chemical interactions for the first five coordination shells. The lattice constant for each concentration is equal to the corresponding experimental value at room temperature.

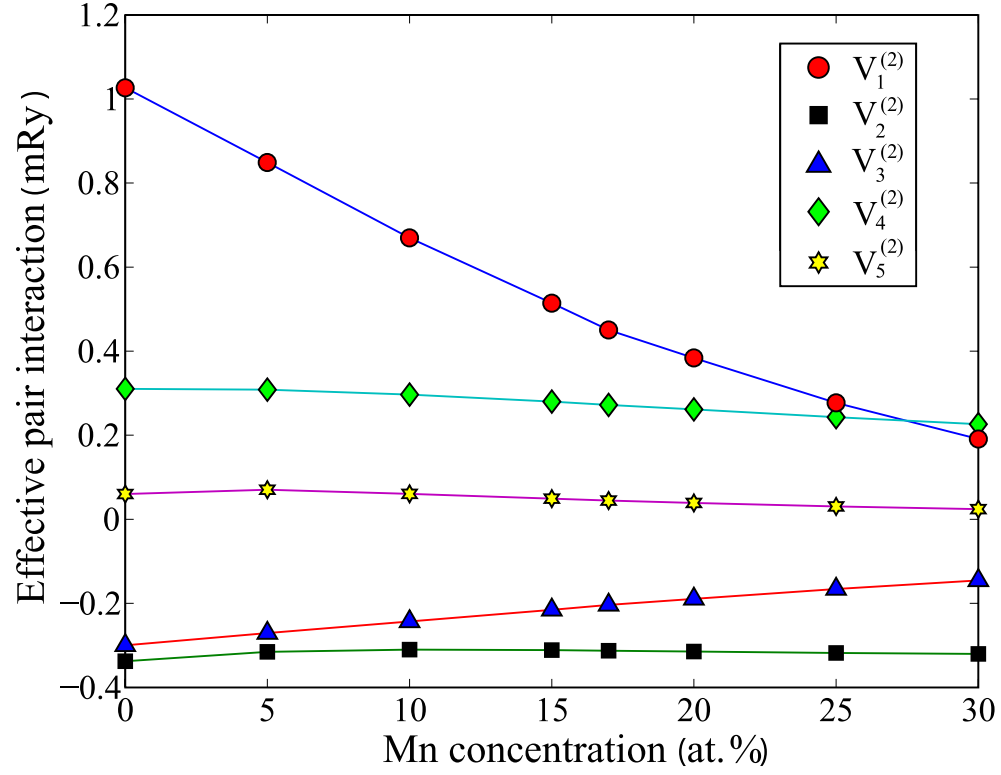


FIG. 3: (Color online) Volume (lattice constant) dependence of the chemical interactions for the first five coordination shells at 17 at% Mn. The dashed line corresponds to the room-temperature value of the lattice constant for this composition.

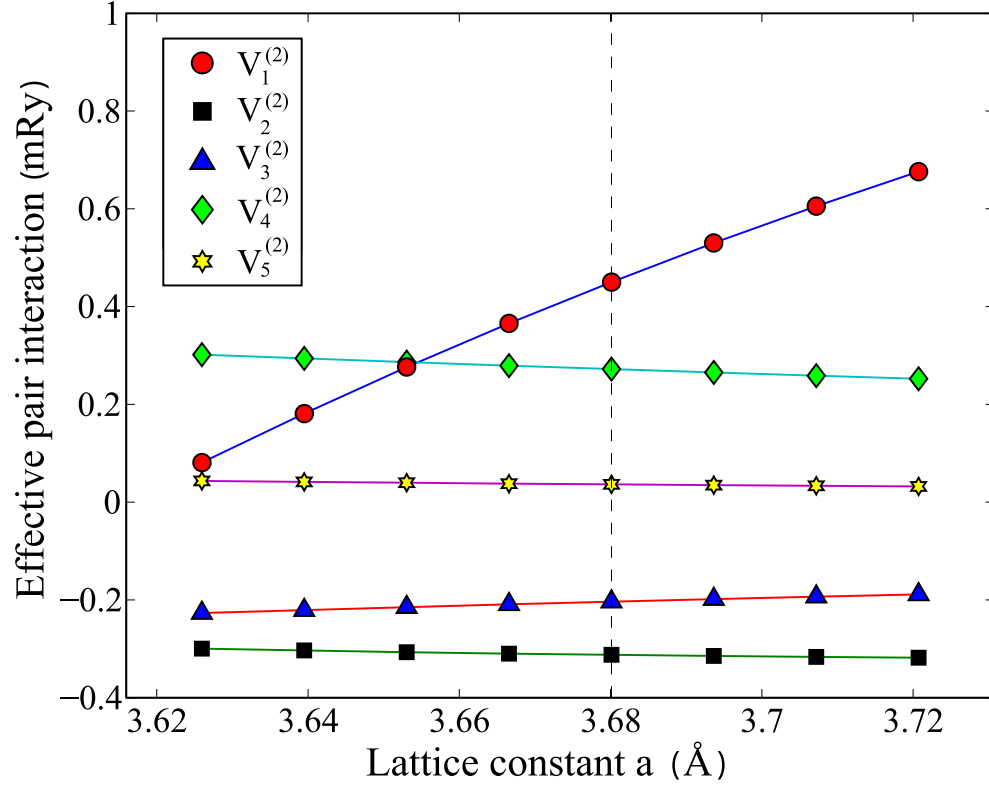


FIG. 4: Left-bottom panel: Fourier transform of the SRO parameters obtained from Monte Carlo simulations for $\text{Cu}_{0.83}\text{Mn}_{0.17}$ at a temperature 500K. Right-top panel: The atomic part of the intensity from a neutron-scattering experiment (Ref. 8). Dark regions correspond to maxima in the intensity; light regions, to minima. Wave vectors are given in reciprocal-lattice units (r. l. u.).

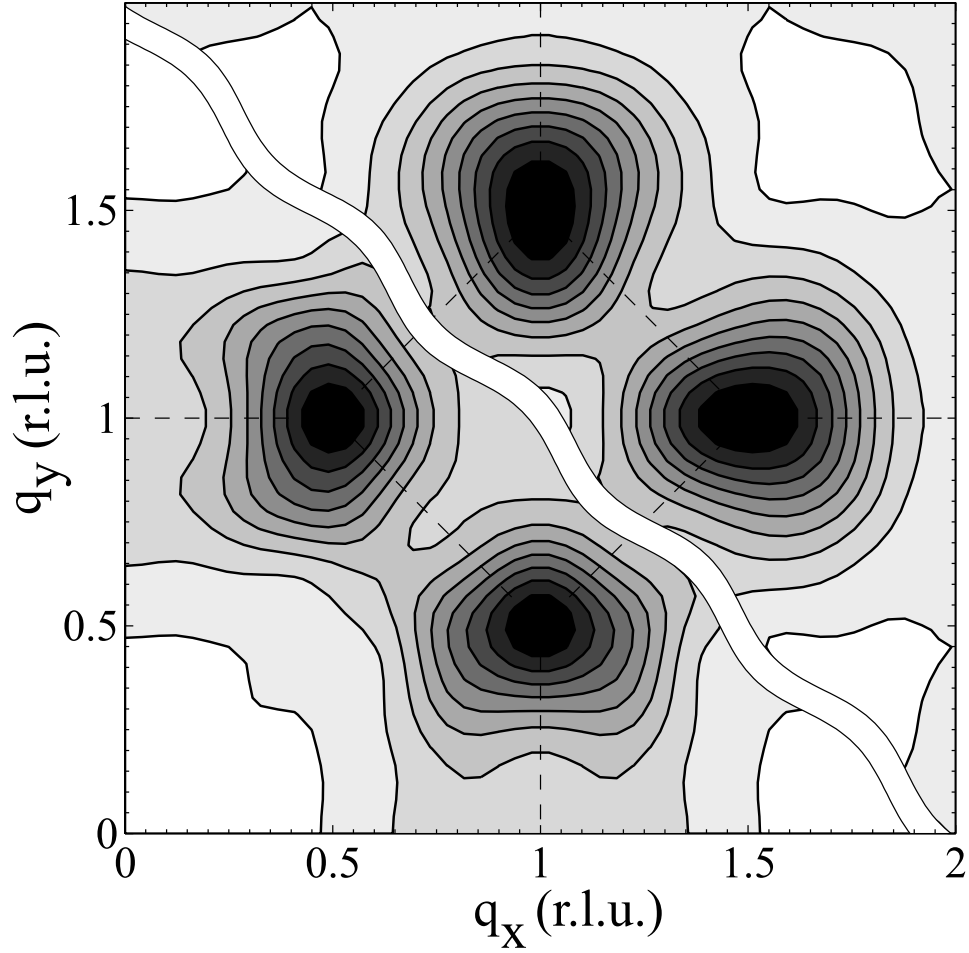


FIG. 5: (Color online) Ordered structure DO_{60} . Light spheres represent the Mn atoms; dark, the Cu atoms. Smaller and larger spheres depict, respectively, positions at the corners and at the face centers of an elementary cubic cell. The elementary cell of the ordered structure is marked with a frame.

FIG. 6: Left-bottom panel: Fourier transform of the spin-spin correlation function obtained from Monte Carlo simulations for $\text{Cu}_{0.83}\text{Mn}_{0.17}$ at a temperature 20K. Right-top panel: The magnetic part of the intensity from a neutron-scattering experiment (Ref 8). Dark regions correspond to maxima in the intensity; light regions, to minima. Wave vectors are given in reciprocal lattice units (r. l. u.).

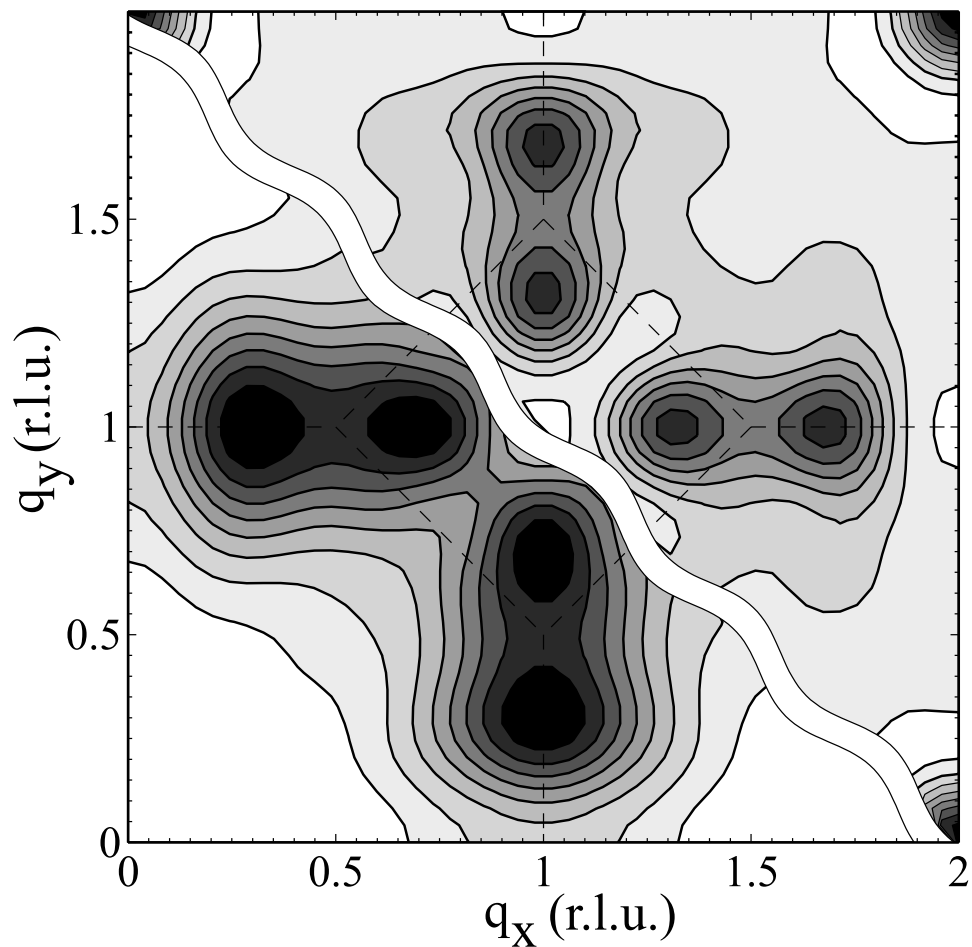


FIG. 7: (Color online) Finite-size scaling of the SG susceptibility.

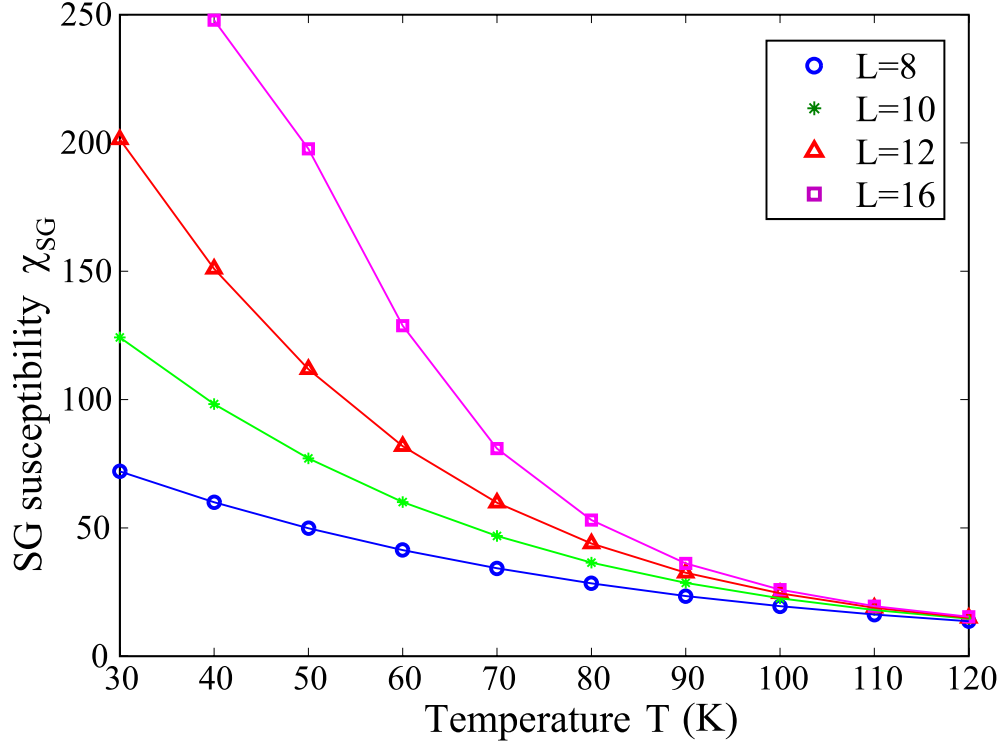


FIG. 8: (Color online) Finite-size scaling of the SG correlation length. Curves for different system sizes cross at $T_c = 57 \pm 5$ K.

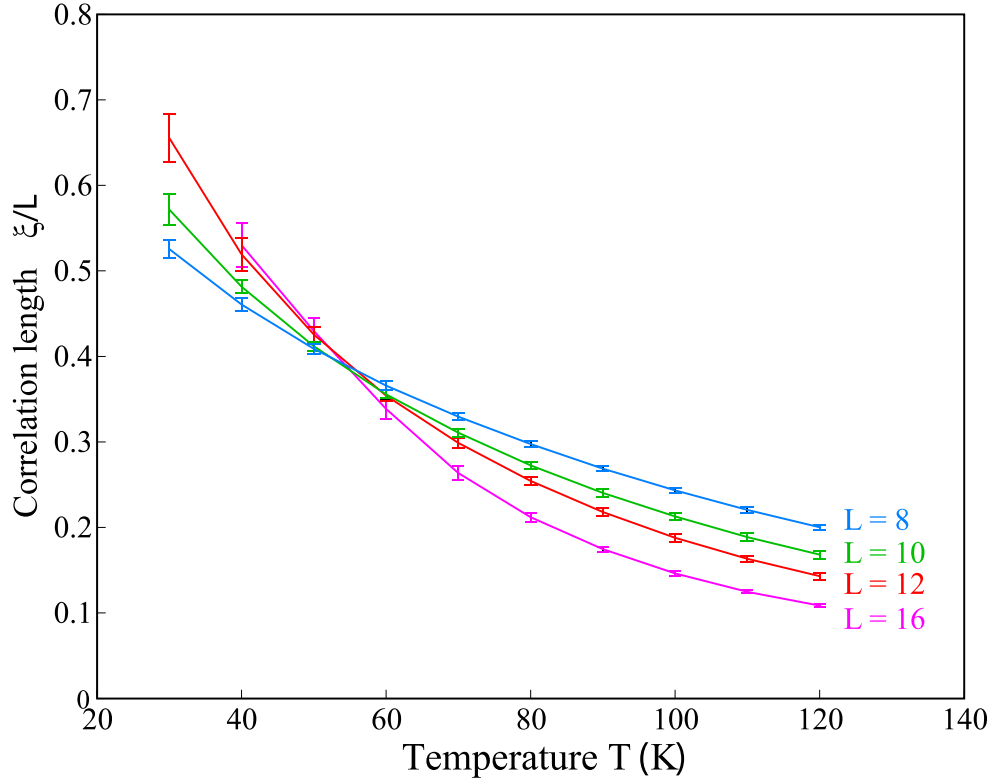


FIG. 9: (Color online) Universal behavior of the SG correlation length. Best fit is achieved with $\nu = 0.95$.

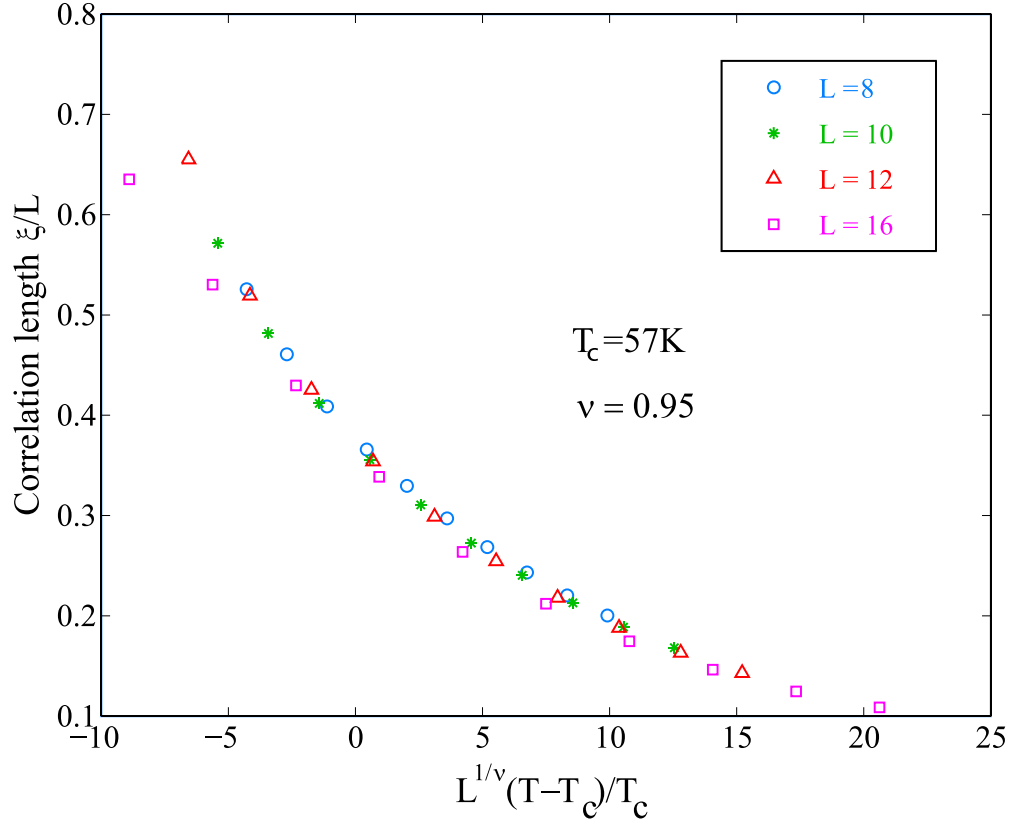


FIG. 10: (Color online) Universal behavior of the SG susceptibility. Best fit is achieved with $\eta = 0.25$.

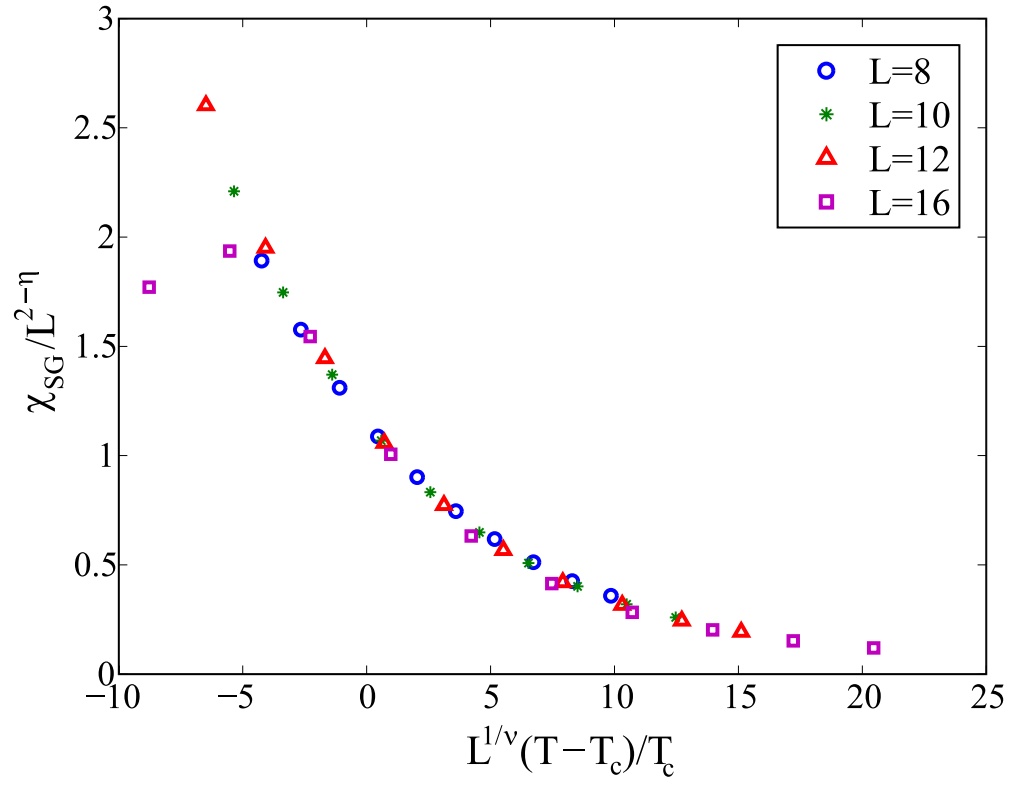


FIG. 11: (Color online) The extended scaling of the SG correlation length according to Eq. (17). The reduced temperature t is defined as $t = T/T_c$.

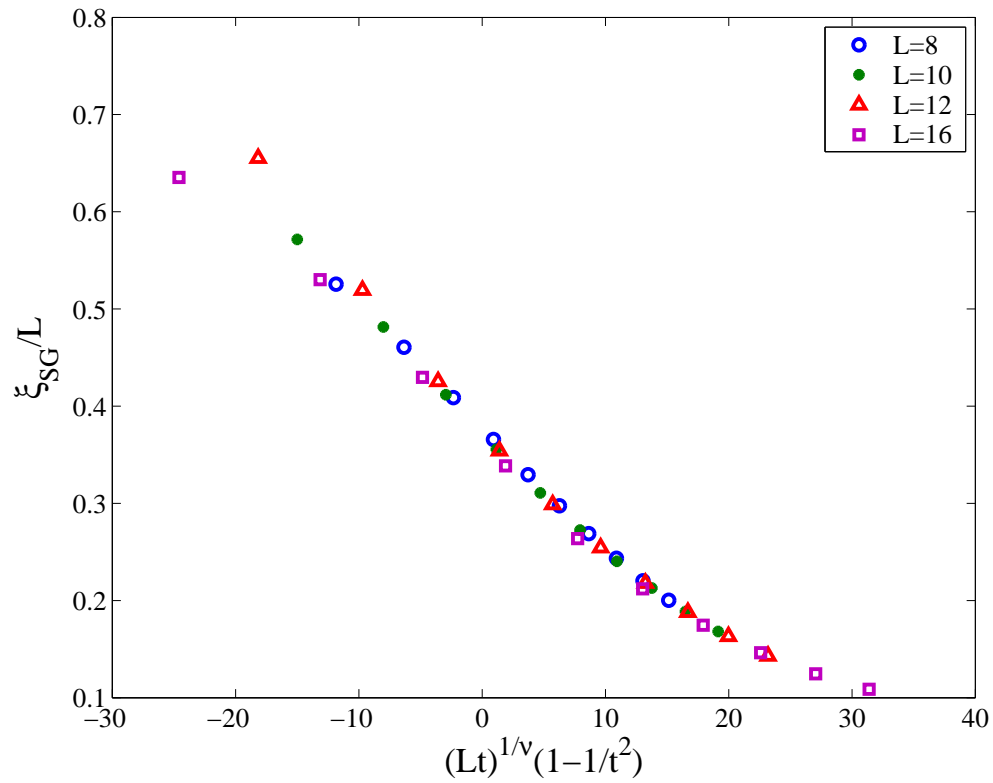


FIG. 12: (Color online) The extended scaling of the SG susceptibility according to Eq. (17). The reduced temperature t is defined as $t = T/T_c$.

